MPE — Volume 2, pp. 205-218
Reprints available directly from the publisher
Photocopying permitted by license only

© 1996 OPA (Overseas Publishers Association)
Amsterdam B.V. Published in The Netherlands
under license by Gordon and Breach Science
Publishers SA
Printed in Malaysia

A SELF-CONSISTENT NUMERICAL METHOD FOR SIMULATION OF QUANTUM TRANSPORT IN HIGH ELECTRON MOBILITY TRANSISTOR; PART I: THE BOLTZMANN-POISSON-SCHRÖDINGER SOLVER

R. KHOIE

Department of Electrical and Computer Engineering, University of Nevada, Las Vegas, Las Vegas, NV 89154

(Received 24 March 1995)

A self-consistent Boltzmann-Poisson-Schrödinger solver for High Electron Mobility Transistor is presented. The quantization of electrons in the quantum well normal to the heterojunction is taken into account by solving the two higher moments of Boltzmann equation along with the Schrödinger and Poisson equations, self-consistently. The Boltzmann transport equation in the form of a current continuity equation and an energy balance equation are solved to obtain the transient and steady-state transport behavior. The numerical instability problems associated with the simulator are presented, and the criteria for smooth convergence of the solutions are discussed. The current-voltage characteristics, transconductance, gate capacitance, and unity-gain frequency of a single quantum well HEMT is discussed. It has been found that a HEMT device with a gate length of 0.7 μm, and with a gate bias voltage of 0.625 V, has a transconductance of 579.2 mS/mm, which together with the gate capacitance of 19.28 pF/cm, can operate at a maximum unity-gain frequency of 47.8 GHz.

KEYWORDS: *Numerical; transport; HEMT; quantum; self-consistent; scattering*

1. INTRODUCTION

Computer modeling of ultra-high speed electron devices, in general, and High Electron Mobility Transistor (HEMT), in particular, remains a main topic of research. With recent advances in device fabrication techniques such as: Molecular Beam Epitaxy (MBE), and Metal Organic Chemical Vapor Deposition (MOCVD), HEMT devices with cutoff-frequencies well in the 300 GHz range have been developed [1]. Along with advances in HEMT fabrication techniques, the need for fast and efficient simulators has continued to increase. The simulation techniques for HEMT devices are based mainly on two different approaches. The computationally intensive Monte Carlo approach [2]–[10], and the hydrodynamic approach with less computational effort and lower degree of accuracy [11]–[13]. Wang and Hess [3] have studied the distribution of electron velocity at high fields using a three-dimensional Monte Carlo, neglecting the quantum effects. Tomizawa, et al. [4] have used two-dimensional scattering rates, and Park, et al. [5] have employed two-dimensional electric field profiles in their Monte Carlo simulations. Price [6], Walukiewicz, et al. [7], Ravaioli and Ferry [8], Tomizawa and Hashizume [9], and Yokoyama and Hess [10] have included the quantum effects in their Monte Carlo programs. More recently, Kizilyalli, et al. [2] have performed a Monte Carlo study of short channel effects in a

submicrometer AlGaAs/GaAs MODFET and suggested that the high frequency performance of the device can be improved by scaling the gate length down to a minimum of about 0.1 μm, beyond which the device transconductance is degraded rather rapidly.

An alternative approach for characterizing the HEMT is using two-dimensional numerical models in which Boltzmann transport and Poisson equations are solved numerically [11]–[13]. Widiger [11] has taken into account the electron heating phenomenon by using hydrodynamic-like transport equations, which include the two higher order moments of Boltzmann equation. In Widiger's model the quantum well is treated by using the triangular well approximation in which the electric field in the quantum well is assumed constant, and the quantized electrons are assumed to reside right at the heterojunction and form a 2-dimensional electron gas (2DEG) with zero width.

The electron energy states in the quantum well are described by Schrödinger equation. Schrödinger equation involves the electrostatic potential in the quantum well which itself depends on the electron concentration in the quantum well. Consequently, obtaining an accurate estimate of electron density in the quantum well requires a self-consistent solution of Poisson and Schrödinger equations. Self-consistent models have been proposed by other researchers [10] and [14]. Yokoyama and Hess [10] have used self-consistent solutions of Schrödinger and Poisson equations to calculate the electron states in the quantum well. Voinigescu [14] has applied a similar self-consistent model to a MODFET with arbitrary band geometry.

This paper presents a Boltzmann-Poisson-Schrödinger solver [15] and [16] which incorporates the effect of the quantization of the electrons in the 2DEG of the quantum well. In Part I of this work, we consider the quantization of the electrons in the first subband. In Part II [17] of this work, we extend our model to a full quantum approach which includes the quantum transport of the electrons in the higher subbands.

2. THE BOLTZMANN-POISSON-SCHRöDINGER SOLVER

The HEMT structure illustrated in Fig. 1 has been considered for the simulation. The gate length is 0.5 μm and on the two sides of the gate are two 0.5 μm regions separating the gate from the source and drain. Beneath the gate is a highly doped $Al_{0.3}Ga_{0.7}As$ layer of width 50nm and doping level of $5.10^{17} cm^{-3}$. Both the gate length and the impurity doping level in the AlGaAs layer are varied in order to investigate the effects of such variations on the performance of the device. A 10nm undoped AlGaAs spacer lies between the highly doped AlGaAs layer and the GaAs layer. Such spacer is included to separate the free electrons in the GaAs channel from their donor impurities in AlGaAs, thereby reducing the remote scattering of electrons by ionized impurities.

The GaAs region consists of a quantum well of width 100nm and a bulk layer of width 300nm, with the two layers overlapping each other as is shown in Fig. 1. The doping level of GaAs is $10^{14} cm^{-3}$. On the two sides are boundaries to two highly-doped GaAs regions, serving as ohmic contacts to the source and drain.

2.1. Boltzmann Transport Equation

The two higher moments of Boltzmann equation consisting of a continuity equation, describing the transport of electrons, and an energy balance equation, describing the

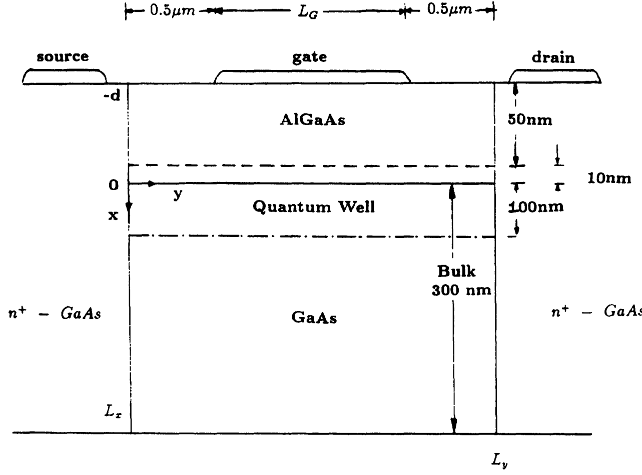

Figure 1. The HEMT structure used in the simulation. The quantum well and the bulk regions overlap each other with a total width of 300 *nm*.

spatial and temporal variation of the average electron energy in the device are given by:

$$\frac{\partial n_b}{\partial t} = \nabla_b \cdot [-\mu_b n_b \nabla_b V + \nabla_b (D_b n_b)] + G_b \tag{1}$$

and

$$\frac{\partial n_b E_b}{\partial t} = -\mathbf{j}_b \cdot \nabla_b V - n_b B_b + \nabla_b \cdot \alpha[-\mu_b n_b E_b \nabla_b V + \nabla_b (D_b n_b E_b)] + F_b, \tag{2}$$

for the bulk, and by:

$$\frac{\partial n_{qw}}{\partial t} = \nabla_{qw} \cdot [-\mu_{qw} n_{qw} \nabla_{qw} V + \nabla_{qw} (D_{qw} n_{qw})] + G_{qw} \tag{3}$$

and

$$\frac{\partial n_{qw} E_{qw}}{\partial t} = -\mathbf{j}_{qw} \cdot \nabla_{qw} V - n_{qw} B_{qw} + \nabla_{qw} \cdot \alpha[-\mu_{qw} n_{qw} E_{qw} \nabla_{qw} V + \nabla_{qw} (D_{qw} n_{qw} E_{qw})] + F_{qw}, \tag{4}$$

for the quantum well. The subscripts b and qw denote the bulk and the quantum well systems, respectively. The bulk and quantum systems and their modeling are described in detail in Section 2.3. In Equations (1) through (4), the terms n and $\mathbf{j}$ are the electron concentration and current density, V is the potential, E is average electron density, μ is the mobility, D is the diffusion constant, and B is the energy dissipation factor. The term G is a generation-like term which is used for redistributing the electrons between the bulk and

the quantum system, and the term F is to account for energy transfer between the two systems. The coefficient α is the ratio of flux mobility to carrier mobility and is given by:

$$\alpha = \frac{\mu_E}{\mu} = \frac{<\tau E_i^2>}{<\tau E_i><E_i>} \tag{5}$$

where τ is the momentum relaxation time, E_i is the electron energy, and the brackets in Eq. (5) refer to statistical averages over the entire sample. For a power-law scattering $\alpha = \frac{2}{3}(p + \frac{5}{2})$, where the power-law scattering is defined as $\tau \propto E_i^p$. For polar optical phonons in GaAs, p has a value of 0.5. In derivation of the above equations it is assumed that the high frequency terms in Boltzmann moment equations are negligible because the high frequency parameter, τ_{HF}, is of the order of 0.1 ps, whereas the typical calculated transient time is of the order of 3 ps.

2.2. Poisson Equation

The above transport equations are solved along with Poisson equation:

$$\frac{\partial^2 V}{\partial x^2} + \frac{\partial^2 V}{\partial y^2} = -\frac{q}{\epsilon}[N_D(x, y) - n(x, y)]. \tag{6}$$

where V is the electrostatic potential, ϵ is the dielectric constant, n is the total electron concentration in the channel, and N_D is the impurity doping level.

2.3. Schrödinger Equation

To model the quantum well, Widiger [11] has employed a triangular well approximation with the assumptions that the electric field in the quantum well is constant, and that the electrons in the 2DEG reside right at the heterojunction. In this paper we take into account the quantization of electron energy levels and the spatial spread of the electrons in the quantum well by means of a self-consistent solution of Schrödinger equation:

$$-\frac{\hbar^2}{2m_x}\frac{d^2\psi_i(x)}{dx^2} - qV(x, y)\psi_i((x) = E_i\psi_i(x) \tag{7}$$

where m_x is the electron effective mass in the x-direction, ψ_i is the wavefunction corresponding to the eigenvalue E_i for the i-th subband, and $V(x, y)$ is the electrostatic potential. The boundary conditions are that the wavefunctions vanish at both infinities. Schrödinger equation is solved using a Rayleigh-Ritz variational method. [18]

To model the quantum well, one possible approach is to define an artificial boundary across the GaAs region, separating the bulk system from the quantized system. Electrons confined by such artificial boundary and the heterojunction are considered to be quantized and their motion is restricted to the y-direction; whereas electrons lying below the artificial boundary are considered as bulk carriers with no restriction to their motion. There are a

number of shortcomings associated with such an approach. First, there is no definite rule to define the quantum well/bulk boundary. As the wavefunction spans over a relatively wide region in the quantum well, if the well width is taken too small, much of the wavefunction outside the boundary will be truncated and the quantum effects can be greatly distorted. On the other hand, if the well width is taken sufficiently large to include a significant portion of the wavefunction, the bulk electronic behavior will be neglected. Neither case is desirable from a device simulation standpoint. Second, the electron concentration over the quantum well/bulk boundary is in general discontinuous, which gives rise to large diffusion current across the boundary. This can cause erroneous results in the simulation. Third, at points where the electric field at the heterojunction is weak, the quantum well is too shallow to confine the electrons and the electrons at the heterojunction behave essentially as bulk carriers. Therefore, it is important that both the bulk and the quantum characters of the electrons are considered, particularly at the heterojunction where the concentration of electrons is the highest.

We present here a different approach to the problem. In this approach, there is no artificial boundary separating the bulk GaAs from the quantum well. Instead, the two systems overlap each other as shown in Fig. 1. The quantum well and the bulk systems both starts at $x = 0$. The quantum well (electrons residing in the lowest subband, E_1) spreads a distance d into the GaAs layer as shown in Fig. 2. The width of the quantum well is determined from the wavefunction for the lowest subband. The bulk system (electrons residing in the second subband, E_2, and higher subbands) extends 300 *nm* into the GaAs layer. Because of this overlapping of the two systems, the electrons at any point across the channel can be in the quantum well or in the bulk, depending on their eigenenergies and the width of the quantum well at that point. Electrons in the bulk undergo transport in both the x- and y-directions whereas electrons in the quantum well are restricted to transport in the y-direction only.

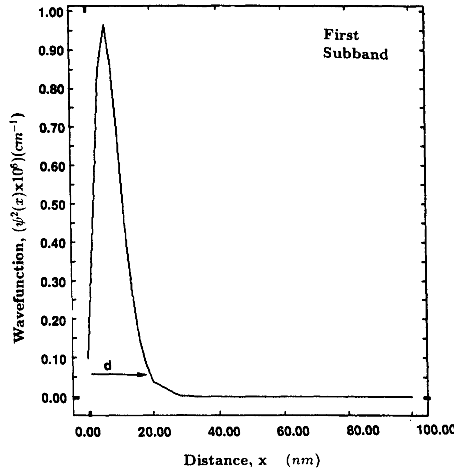

Figure 2. Calculated wavefunction, $\psi_1(x)^2$, of the first subband at 300°*K* with an applied gate voltage of 0.5 V and a drain bias of 1.5 V for Device II. The wavefunction peaks at 7 *nm* from the interface and spreads about 20 *nm* in the *GaAs* layer.

Yokoyama and Hess [10] have reported that at 77°K, 98 percent of electrons in the quantum well are residing in the first subband whereas at 300°K, the population of electrons residing in the first subband reduces to 68 percent. In spite of this fact, in Part I of this work we consider only the quantization of electrons in the lowest subband. Part II of this work [17] presents a full quantum approach in which the quantization of electrons in the higher subbands is incorporated.

The transport of electrons in the device is governed by six coupled, nonlinear partial differential equations (1), (2), (3), (4), (6), and Schrödinger equation (7), with the unknown variables n_{qw}, E_{qw}, n_b, E_b, V, and $\psi_i(x)$, E_i. The system of equations consisting of these six equations is solved iteratively by using a 2-dimensional finite difference scheme. In each iteration cycle the values of the variables n_{qw}, E_{qw}, n_b, E_b, V, and $\psi_i(x)$, E_i are updated until the correction terms to these variables are within a tolerance range. It should be noted that the Schrödinger equation is solved at each (x, y) point and the values of the wavefunctions and the eigenenergies are updated in each iteration cycle.

2.4. Numerical Stability Considerations

The numerical solution of the partial differential equations outlined above requires iterative computation both in time and space. Numerical instability problems are often associated with such iterative process and careful consideration is needed to ensure smooth convergence of the results.

An explicit approach is commonly employed to solve the continuity equation:

$$\frac{\partial n}{\partial t} = \frac{1}{q} \nabla \cdot \mathbf{J} + G, \tag{8}$$

which is discretized into the form:

$$n^{k+1} = n^k + \Delta t \left(\frac{1}{q} \nabla \cdot \mathbf{J}^k + G^k \right). \tag{9}$$

The values of n, $\mathbf{J}$, and G at time k are plugged into the right-hand-side of Eq. (9) yielding the value of n at the next time step $k + 1$. This method is extremely straight forward requiring no complex matrix operation. However, the major drawback of this approach is that excessively small time steps are required to guarantee numerical stability. Specifically, it has been shown [19] that the maximum time step one can use without having any instability problem is:

$$\Delta t < \min \left[\frac{\Delta x^2 \Delta y^2}{2D(\Delta x^2 + \Delta y^2)}, \frac{2D}{v_\infty^2} \right], \tag{10}$$

where Δx and Δy are the mesh spacings, D the diffusivity, and v_∞ the saturation velocity. When the time step Δt exceeds the value given by Eq. (10), a minor perturbation in the values of $n_{i,j}$ at mesh point (i, j) can result in a diverging solution. The smallest mesh dimensions Δx and Δy in this simulation are $2 \cdot 10^{-7}$ cm and $5 \cdot 10^{-6}$ cm, respectively. The

diffusivity at low field is about 300 cm^2/s. Assuming the mesh spacing to be the limiting factor to the speed of the iterative process, the maximum time step one can use without causing numerical instability is: (for all values of v_∞)

$$\Delta t < 6.10^{-17}\, sec.$$

which is of the order of 10^6 times smaller than the typical transient time of HEMT. This poses a serious problem for the convergence of the program.

In order to increase the time step to speed up the program, one has to increase the mesh spacing which in turn will sacrifice the accuracy of the result. Another approach to the solution of the continuity equation is to write the equation in an implicit form:

$$\frac{\partial n}{\partial t} = \frac{1}{2q}[\nabla \cdot \mathbf{J}^k + \nabla \cdot \mathbf{J}^{k+1}] + G^k. \tag{11}$$

where the superscript k represents time. The price to pay is complicated discretization and tedious solution. In this paper, the implicit approach based on Eq. (11) is used.

The time step size used in our simulations is $1.0 \cdot 10^{-15}$ sec. The spatial mesh employed has nonuniform mesh spacing in the x-direction with mesh sizes, Δx, ranging from $2 \cdot 10^{-7}$ cm to $5 \cdot 10^{-6}$ cm. The mesh sizes are smaller in the proximity of the heterojunction. The mesh spacing in the y-direction, Δy, is uniform with a mesh size of $5 \cdot 10^{-6}$ cm. This mesh spacing is for a device with gate length of 0.7 μm. The mesh spacing Δy is adjusted as the gate length is varied.

3. RESULTS

Computer simulations have been performed on five different HEMT's with various device structures at room temperature. The design parameters of these devices are tabulated in Table 1. Devices I, II and III have the same doping level of $5 \cdot 10^{17}$ cm^{-3} in the AlGaAs, but have different gate lengths: 0.5, 0.7, and 1.0 μm, respectively. Devices IV and V are simulated with the same gate length of 0.7 μm but different doping levels: $2.5 \cdot 10^{17}$ cm^{-3} and $7.5 \cdot 10^{17}$ cm^{-3}, respectively. The results presented in Figures 2 through 6 are in reference to Device II.

Table 1 Design parameters of the HEMT devices simulated

Device	*Gate Length (μm)*	*Channel Length (μm)*	*AlGaAs Thickness nm*	*AlGaAs Doping (cm^{-3})*	*GaAs Doping (cm^{-3})*	*Temp. (K)*
I	0.5	1.5	60	$5.0 \cdot 10^{17}$	10^{14}	300
II	0.7	1.7	60	$5.0 \cdot 10^{17}$	10^{14}	300
III	1.0	2.0	60	$5.0 \cdot 10^{17}$	10^{14}	300
IV	0.7	1.7	60	$2.5 \cdot 10^{17}$	10^{14}	300
V	0.7	1.7	60	$7.5 \cdot 10^{17}$	10^{14}	300

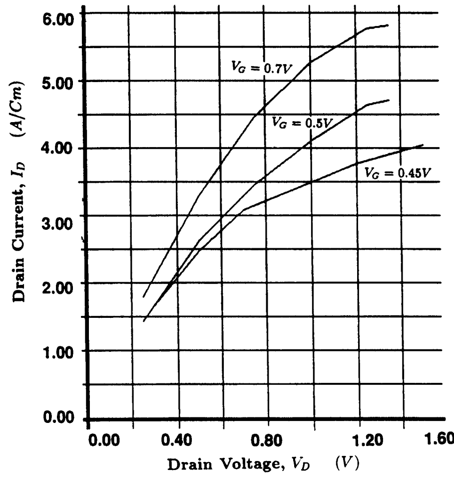

Figure 3. $I_D - V_D$ characteristics of Device II under different gate biasing conditions.

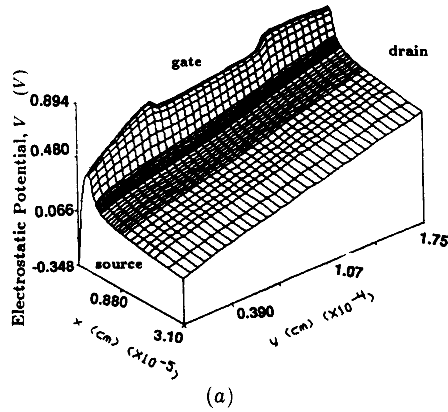

(a)

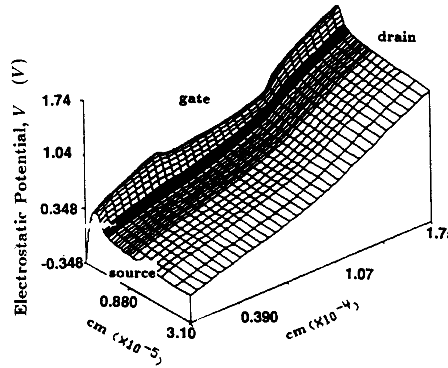

(b)

Figure 4. Electrostatic potential profiles for Device II with a gate voltage of 0.7 V and drain voltage of (a) 0.5 V, and (b) 1.35 V.

Fig. 2 shows the square of the wavefunction, $\psi_1(x)^2$, for the first subband with an applied gate voltage of 0.5 V and a drain bias of 1.5 V. The function $\psi_1(x)^2$ peaks at about 7 *nm* from the interface to a value of about $96 \cdot 10^4\ cm^{-1}$. The spatial spread of the well is 20 *nm*. The calculated eigenenergies for the first and second subbands are 46 and 69 meV, respectively. These results are in good agreement with those reported by Yokoyama and Hess [10].

Fig. 3 shows the $I_D - V_D$ characteristics of Device II under three different gate bias of 0.45 V, 0.5 V, and 0.7 V. The linear and the saturation regions can be identified on the $I_D - V_D$ characteristics, in which the onset of saturation occurs between 0.7 V and 1.2 V, depending on the gate bias. The output resistance at $V_D = 1V$ and $V_G = 0.45V$ is approximately 7 Ω.mm. At a gate voltage of 0.5V the output resistance decreases to 4 Ω.mm, which is less than the typical reported measurements. This discrepancy can be attributed to the assumed ideal contact behavior at the drain and source boundaries.

Fig. 4 shows the electrostatic potentials in the device with a gate voltage of 0.7 V and two drain biases of 0.5 V and 1.35 V. Fig. 5 shows the electron concentrations in the quantum well and the bulk GaAs under the same biasing conditions. The electron concentration in the quantum well are calculated by multiplying the electron sheet density in the quantum well by the probability density, $\psi_1(x)^2$. In the case of $V_D = 0.5$ V, the

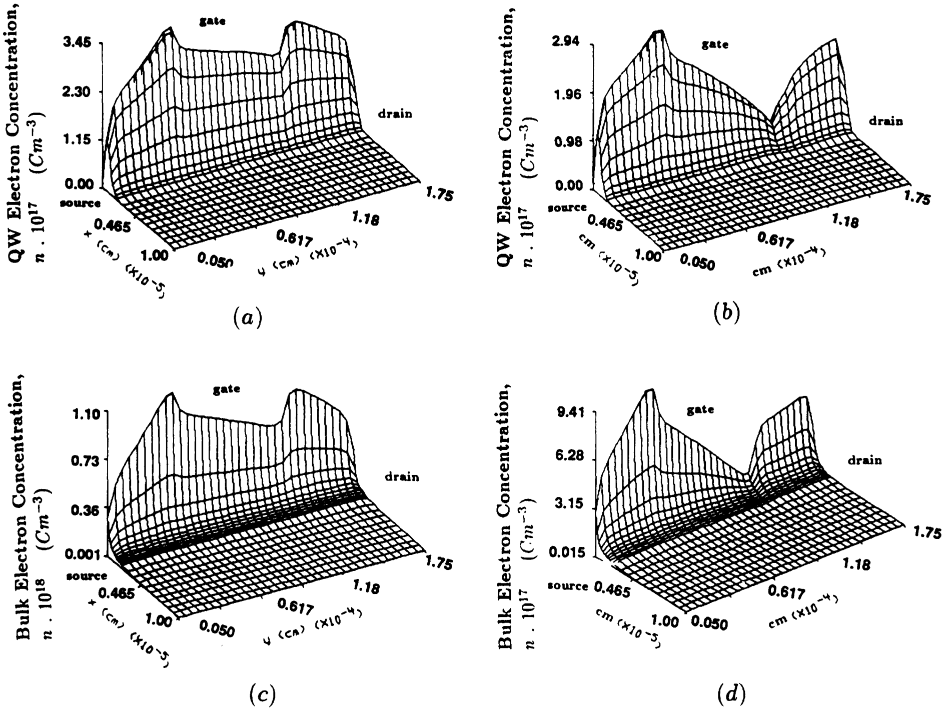

Figure 5. Electron concentrations in (a,b) quantum well and (c,d) bulk *GaAs* of Device II. The applied gate voltage is 0.7 V in all cases. The drain bias is 0.5 V in (a) and (c) and 1.35 V in (b) and (d). The concentration of the electrons in the quantum well is obtained by multiplying the probability density, $\psi_1(x)^2$, by the electron sheet density. The quantum well spreads about 200 $A°$ into the *GaAs* layer whereas the active bulk extends 1000 $A°$ into the GaAs layer.

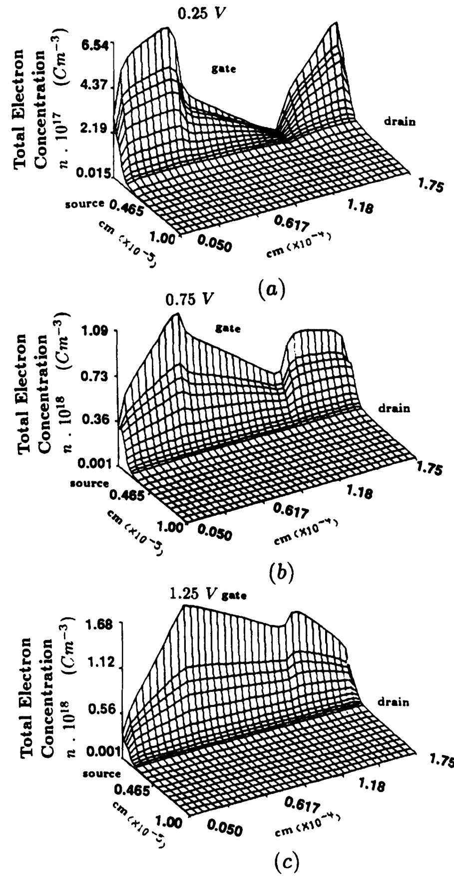

Figure 6. Total electron concentration in Device II with a drain voltage of 0.9 V and a gate voltage of (a) 0.25 V, (b) 0.75 V, and (c) 1.25 V.

electron concentrations in the quantum well and the bulk *GaAs* are relatively uniform from source to drain, whereas in the case of $V_D = 1.35$ V, there is a sharp reduction in the electron concentration in the region underneath the drain end of the gate which is the pinch-off point. Also shown in Fig. 5 are the spatial spreading of the quantum well and the bulk systems. It should be noted that while the concentration of electrons in the quantum well reduces to zero at a distance of 200 $A°$ from the interface (Fig. 5a), the concentration of electrons in the bulk system reduces to $15 \cdot 10^{14}$ (approaching the doping level of the bulk GaAs, See Fig. 5c) at a distance of 1000 $A°$ from the interface. It is thus concluded that the width of the quantum well is about one fifth of the conduction channel.

We have studied the effects of the applied gate voltage on the electron transport in the GaAs channel by simulating the operation of Device II under a fixed drain voltage of 0.9 V and various gate voltages ranging from 0.25 V to 1.25 V. Fig. 6 shows the total electron concentrations in Device II under three different gate biasing conditions. The electron

concentration in the conduction channel under the gate increases with the gate voltage as expected. The pinch-off phenomenon, as indicated by the valley in Fig. 6a, is pronounced in the case of the 0.25 V gate bias. This is because the drain voltage is much higher than the gate voltage. Electrons in the channel are largely drawn toward the drain contact, resulting in a slightly depleted region underneath the gate, which is the pinch-off point. As higher gate voltages are applied, the pinch-off point disappears, as clearly demonstrated in Figs. 6b and 6c.

The drain current-gate voltage ($I_D - V_G$) characteristics for Devices I–V are given in Fig. 7a. We also calculate the total charge in the device by integrating over the entire GaAs region the sum of the bulk and the quantum well electron concentrations: $Q = \int_0^{L_y}\int_0^{L_x} q \cdot n(x, y)dxdy$. Fig. 7b shows the variations in the total charge in the GaAs layer

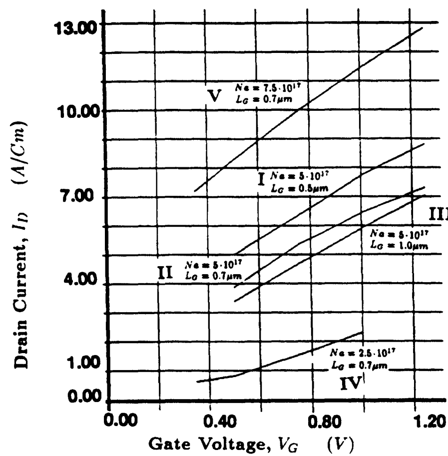

(a)

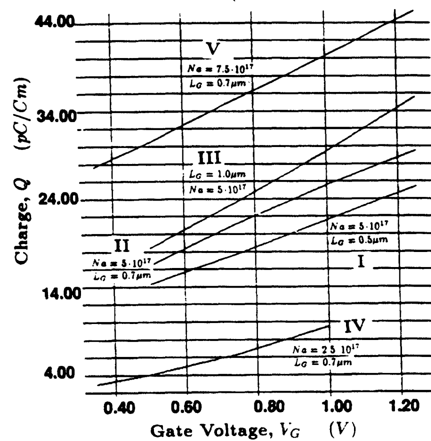

(b)

Figure 7. (a) Drain current-gate voltage characteristic and (b) channel charge-gate voltage characteristics of Devices I–V under a drain bias of 1.0 V.

with the applied gate voltage. The total charge in GaAs increases with increasing channel lengths (Devices I, II and III) and with increasing doping level in AlGaAs (Devices IV, II and V). The former result agrees with the general consideration that a device with longer channel length would have more charge in the GaAs layer. The latter result is due to the fact that variation in the doping concentration in AlGaAs causes variation in the electric field built up at the heterojunction and thus the amount of charge induced in the GaAs channel.

Based on the above results, we obtain values of the transconductance, the gate capacitance, and the unity-gain frequency according to the following formulae: $g_m = \frac{\partial I_d}{\partial V_g}$, $C_g = \frac{\partial Q}{\partial V_g}$, and $f_T = \frac{1}{2\pi}\frac{g_m}{C_g}$. The transconductance as a function of gate voltage for the five devices simulated under a fixed drain bias of 1 V are shown in Fig. 8a. The graphs show a general pattern in which the transconductance increases with the gate voltage at low gate bias; however, as the gate bias is raised further, the transconductance levels off and

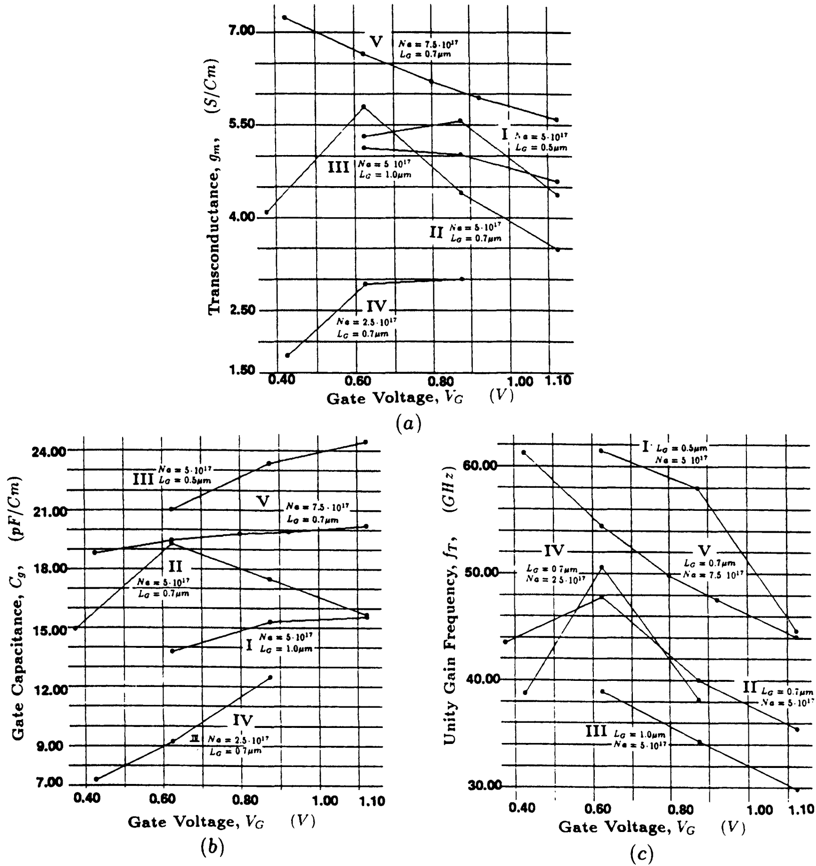

Figure 8. (a) Transconductance, (b) gate capacitance, and (c) unity-gain frequency of Devices I–V as a function of gate voltage. The drain bias is 1.0 V.

then starts to decrease. Similar patterns are observed in the plots of the gate capacitance (Fig. 8b) and the unity-gain frequency (Fig. 8c). One reason for the drop of the transconductance and the gate capacitance as the gate voltage is increased, is that the electron concentration in the channel is limited by the supply of electrons at the source boundary. As a result, the electron concentration and thus the current density in the channel do not increase proportionally with the gate voltage. For Device II, the maximum transconductance obtained is 579.2 mS/mm at a gate bias of about 0.625 V. The gate capacitance at such gate bias is 19.28 pF/cm and the resulting unity-gain frequency is 47.8 GHz.

4. CONCLUSIONS

A Boltzmann-Poisson-Schrödinger Solver for High Electron Mobility Transistor was discussed with consideration of quantization of the electron energy levels at the heterojunction and spatial spreading of electrons in the quantum well. It has been found that the ratio of the finite width of the quantum well to the width of the active channel can be as high as 0.2. The assumptions of the quantum well with zero width, and the quantized electrons residing right at the heteroface clearly become invalid. The pinch-off phenomenon and the two-dimensional nature of electron transport have been demonstrated. A maximum transconductance of 531.2 mS/mm for a HEMT with gate length of 0.5 μm and a doping level of $5 \cdot 10^{17}\ cm^{-3}$ has been obtained, which has corresponding gate capacitance and unity-gain frequency of 13.8 pF/cm and 61.5 GHz, respectively.

The values of the transconductance and the unity-gain frequencies obtained from these HEMT simulations are somewhat larger than reported by [12] and [13]. In Part II [17] of this work we correct this overestimation by extending our model to include the quantization of electrons in the higher subbands. We also add an additional self-consistency by calculating the transport parameters as a function of energy and electric field.

References

1 L.D. Nguyen, A.S. Brown, M.A. Thompson, and L.M. Jelloian, "50-nm Self-Aligned-Gate Pseudomorphic AlInAs/GaInAs High Electron Mobility Transistors", *IEEE Transactions on Electron Devices*, Vol. 39, No. 9, pp. 1007–2014, 1992.

2 I.C. Kizilyalli, M.A. Artaki, N.J. Shah, and A. Chandra, "Scaling Properties and Short-Channel Effects in Submicrometer AlGaAs/GaAs MODFET's: A Monte Carlo Study", *IEEE Trans. Electron Devices*, vol. ED-40, pp. 234–249, 1993.

3 T. Wang and K. Hess, "Calculation of the Electron Velocity Distribution in High Electron Mobility Transistors Using an Ensemble Monte Carlo Method," *Journal of Applied Physics*, vol. 57, pp. 5336–5339, 1985.

4 M. Tomizawa, A. Yoshii, and K. Yokoyama, "Modeling for an AlGaAs/GaAs Heterostructure Device Using Monte Carlo Simulation," *IEEE Electron Device Letters*, vol EDL-6, pp. 332–334, 1985.

5 D. Park, Y. Wang, and K.F. Brennan, "Ensemble Monte Carlo Simulation of a 0.35-μm Pseudomorphic HEMT" *IEEE Electron Device Letters*, vol EDL-10, pp. 107–110, 1989.

6 P. Price, "Electron Transport in Polar Heterolayers," *Surface Science*, vol. 113, pp. 199–210, 1982.

7 W. Walukiewicz, H. E. Ruda, J. Lagowski, and M. C. Gatos, "Electron Mobility in Modulation Doped Heterostructure," *Physical Review B*, vol. 30, pp. 4571–4582, 1984.

8 U. Ravaioli and D. Ferry, "MODFET Ensemble Monte Carlo Model Including the Quasi-Two-Dimensional Electron Gas," *IEEE Transactions on Electron Devices*, vol. ED-33, pp. 677–680, 1986.

9 K. Tomizawa and N. Hashizume, "Ensemble Monte Carlo Simulation of an *AlGaAs/GaAs* Heterostructure MIS-Like FET," *IEEE Transactions on Electron Devices*, vol. ED-35, pp. 849–856, 1988.
10 K. Yokoyama and K. Hess, "Monte Carlo Study of Electronic Transport in $Al_{1-x}Ga_xAs/GaAs$ single-well heterostructures," *Physical Review B*, vol. 33, pp. 5595–5606, 1986.
11 D. J. Widiger, I. C. Kizilyalli, K. Hess, and J. J. Coleman, "Two-dimensional Transient Simulation of an Idealized High Electron Mobility Transistor," *IEEE Transactions on Electron Devices*, vol. ED-32, 1092–1102, 1985.
12 I. C. Kizilyalli, K. Hess, J. L. Larson, D. J. Widiger, "Scaling Properties of High Electron Mobility Transistor," *IEEE Trans. Electron Devices*, vol. ED-33, pp. 1427–1432, 1986.
13 D. Loret, "Two-dimensional Numerical Model for the High Electron Mobility Transistor," *Solid-State Electronics*, vol. 30, pp. 1197–1203, 1987.
14 S. Voinigescu, "Quantum Modeling of Charge Distribution in Single and Multiple Heterojunction MODFETs," *International Journal of Electronics*, vol. 66, no. 2, pp. 227–245, 1989.
15 Z. H. Ng, R. Khoie, and R. Venkat, "A Two-Dimensional Self-Consistent Numerical Model for High Electron Mobility Transistor", *IEEE Transactions on Electron Devices*, Vol. 38, No. 4, pp. 852–861, 1991.
16 Z. H. Ng, R. Khoie, and R. Venkat, "A Self-Consistent Calculation of Spatial Spreading of the Quantum Well in HEMT", *Computational Electronics, Semiconductor Transport and Device Simulation*, edited by: K. Hess, J. Leburton, and U. Ravaioli, Kluwer Academic, pp. 55–58, 1991.
17 R. Khoie, "A Self-consistent Numerical Method for Simulation of Quantum Transport in High Electron Mobility Transistor; Part II: Full Quantum Transport", *Elsewhere in this publication*, 1996.
18 S. H. Gould, *Variational Methods for Eigenvalue Problems*, second ed., Univ. of Toronto Press, 1957.
19 C. M. Snowden, *Semiconductor Device Modelling*. IEE Materials and Device Series 5. Peter Peregrin. London, UK., 1988.